Electronic Supplementary Material (ESI) for Nanoscale.
This journal is © The Royal Society of Chemistry 2020

SUPPLEMENTARY INFORMATION

Unveiling surface charge on chalcogen atoms toward the high aspect-ratio colloidal growth of two-dimensional transition metal chalcogenide

Yunhee Cho,[a,b] Thi Anh Le,[a,b] Hyunjung Kim,[a,c] Yeseul Hong,[a,b] Heemin Hwang,[a,d] G. Hwan Park,[a,b] Sohyeon Seo,[a] and Hyoyoung Lee*[,a,b,c]

[a]*Center for Integrated Nanostructure Physics (CINAP), Institute for Basic Science (IBS), Sungkyunkwan University, 2066 Seoburo, Jangan-gu, Sown, Gyeonggi-do, 440-746, Republic of Korea.*

[b]*Department of Chemistry, Sungkyunkwan University, 2066 Seoburo, Jangan-gu, Sown, Gyeonggi-do, 440-746, Republic of Korea*

[c]*SKKU Advanced Institute of Nanotechnology (SAINT), Sungkyunkwan University, 2066 Seoburo, Jangan-gu, Suwon 16419, Republic of Korea*

[d]*Department of Energy Science, Sungkyunkwan University, 2066 Seoburo, Jangan-gu, Sown, Gyeonggi-do 440-746, Republic of Korea.*

*Email of correspondence: hyoyoung@skku.edu

KEYWORDS colloidal synthesis, two-dimensional nanosheets, ligand cone angle, nucleation stability, growth mechanism

TABLE OF CONTENTS

	Page
Supplementary note 1: Sherrer analysis of the facets	4
Figure S1. Magnification of the (100) diffraction peak in the case of $MoSe_2$ synthesized with TOPO as ligands	4
Figure S2. Characterization of $MoCl_5$-ligand complexes obtained before the injection of selenium precursors	5
Figure S3. XRF data for the amounts of Mo and Se precursors after synthesis of the $MoSe_2$ with Olm and TOPO as ligands	6
Supplementary note 2: Nanosheets growth reaction equilibrium	6-7
Figure S4. (a) Schematic representation of the LaMer diagram for nucleation and growth of $MoSe_2$-TOPO (red line) and $MoSe_2$-Olm (black line)	8
Figure S5. UV-vis absorption spectra of reagents for the synthesis of $MoSe_2$.	8
Figure S6. Atomic force microscopy (AFM) images of $MoSe_2$ synthesized with various concentrations of TOPO	9
Table S1. The height profiles for AFM analysis of $MoSe_2$ synthesized with various Ln of TOPO	10-12
Figure S7. Atomic force microscopy (AFM) images of $MoSe_2$ synthesized with various concentrations of Olm	13
Table S2. The height profiles for AFM analysis of $MoSe_2$ synthesized with various Ln of Olm.	14-16
Figure S8. FTIR spectra of the synthesized $MoSe_2$ nanosheets with (a) TOPO and (b) Olm.	16
Figure S9. Raman scattering spectra of the $MoSe_2$ nanosheets synthesized with Olm and TOPO.	17
Table S3. XPS of the Mo 3d core level	18
Table S4. XPS of the Se 3d core level	18
Figure S10. Thermogravimetric (TG) spectra of the $MoSe_2$ nanosheets synthesized with different organic ligands	19
Figure S11. Photograph of the colloidal nanosheets solution in $CHCl_3$.	20

Figure S12. The XPS spectra of $MoSe_2$ nanosheets grown for 5h with different ligands	20
Supplementary note 3:Detailed calculation methods	21
Table S5. The surface energies of different facets in $MoSe_2$ depending on ligand coverage of trimethylphosphinine oxide (Me_3PO) and methylamine ($MeNH_2$)	22
Figure S13. Model structure for calculations of the surface energies in accordance with the ligand coverage percentage	22-23
Figure S14. The surface energies of (001) facets as a function of the ligand coverage percentage	24
Figure S15. XPS and XRD spectra of the corresponding $MoSe_2$ nanosheets with L5, L100, and L265 of TOPO	24
Figure S16. (a-c) HRTEM images of the $MoSe_2$ synthesized with L5, L50, and L265	25
Figure S17. The crystalline sizes along the (100) and (110) facets according to Ln	25
Table S6. The crystalline size of $MoSe_2$ synthesized with different concentration of TOPO, Ln.	26
Figure S18. Plot of the average lateral size of the $MoSe_2$ nanosheets synthesized with Olm	26
Figure S19. TEM images of $MoSe_2$ synthesized with aliphatic ligands. $MoSe_2$ nanosheets were synthesized with Olm and oleic acid	27
Figure S20. UV-vis spectra of aliquots with (a-e) different amounts of TOPO extracted as a function of time.	28
Table S7. Quantitative analysis of the remaining precursors after reaction as a function of the concentration of TOPO as determined by X-ray fluorescence spectroscopy.	29
Figure S21. TEM images of $MoSe_2$ synthesized with L100 of ligands in the composition of TOPO: phosphine oxide ligands, which have various cone angles	30
Figure S22. TEM images of $MoSe_2$ nanosheets synthesized with 265 equivalents of TOPO for the amounts of chalcogen ions produced by phenyldiselenide	31
Figure S23. HRTEM images of $MoSe_2$ synthesized at 330 °C for 10 hours, with 265	31

equivalents of TOPO	

Supplementary note 1: Sherrer analysis of the facets

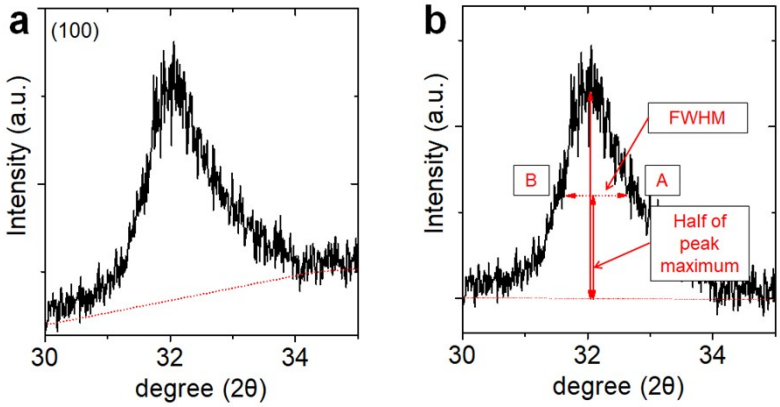

Figure S1. Magnification of the (100) diffraction peak in the case of $MoSe_2$ synthesized with TOPO as ligands (a) before and (b) after subtraction of the baseline for calculating the size of crystallite by Scherrer equation.

The background baseline was subtracted from the raw data to confirm the peak position and the intensity of the peak maximum. Then the half maximum value from A to B (FWHM, Δ 2θ) was calculated. Sherrer's equation is utilized to calculate the size of crystalline grains along the nanosheets for each diffraction pattern directsion of (100) and (110), which corresponds to the lateral growth of the $MoSe_2$ nanosheets. A shape factor of 0.9 is used in the Sherrer equation.

Crystallites' radius = shape factor * wavelength of Cu kα / (FWHM * cos θ)

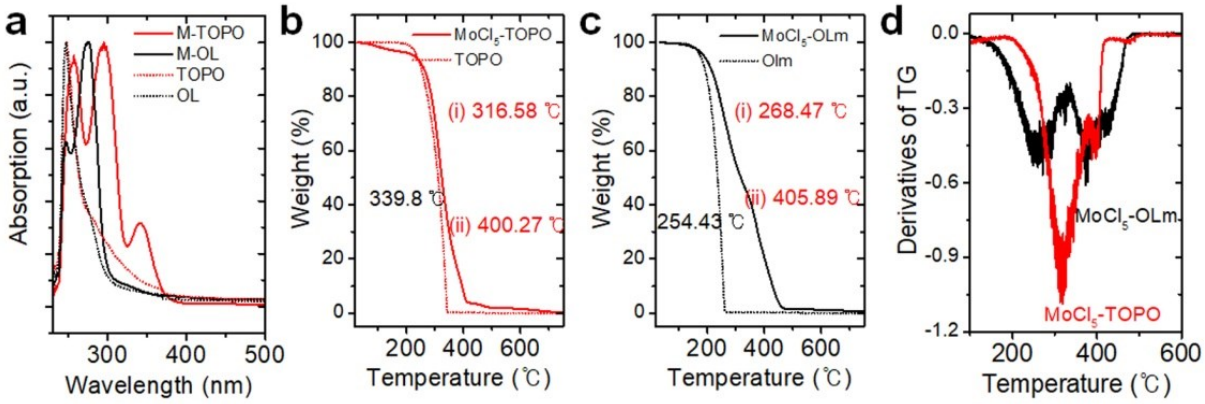

Figure S2. Characterization of $MoCl_5$-ligand complexes obtained before the injection of selenium precursors. (a) UV-vis spectrum of $MoCl_5$-ligand complexes and ligands. Thermogravimetric analysis (TGA) of (b) $MoCl_5$-TOPO and TOPO, (c) $MoCl_5$-Olm and Olm, and (d) and their derivatives. The number (black color) indicates the temperature, where each weight loss with the largest slope was observed using the derivative of the TGA spectrum.

Considering the TGA analysis of ligands (dotted lines in each spectrum), the first thermal decomposition of metal-ligand complexes indicates the physisorption of ligands (i), and the second thermal decomposition of complexes (ii) represents the chemical interactions between the metal cations and ligands.

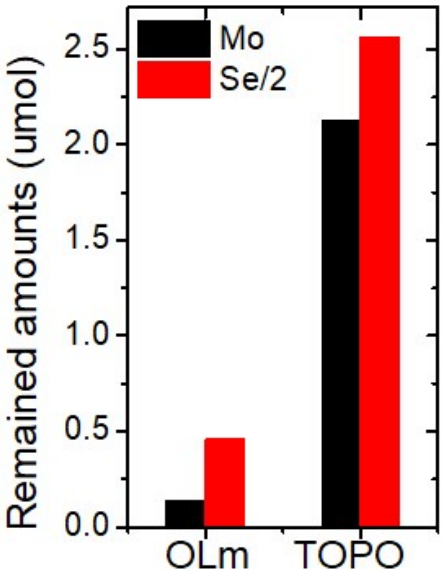

Figure S3. XRF data for the amounts of Mo and Se precursors after synthesis of the $MoSe_2$ with Olm and TOPO as ligands.

Supplementary note 2:

Nanosheets growth reaction equilibrium

For understanding the nanosheet's growth reaction, the nucleation and growth of nanosheets are only considered (equation (3)) without further consideration of the reactant chemical reaction for supplying Mo/Se precursors (equation (2)).

$MoCl_5 + yL \rightarrow MoCl_xL_y + (5-x)/2Cl_2$ (g) ---(1)

$Ph_2Se_2 \rightarrow 2\ PhSe^* \rightarrow 2\ Ph^* + 2\ Se^*$ ---(2)

$MoCl_xL_y + 2\ Se^* + L \leftrightarrow [MoSe_2]_n\text{-}L_{y'}$ ---(3)

$dG = dG_f - dG_i = -SdT + VdP + \sum_{i=0}^{n} \mu_i dN_i$ ---(4)

$dG \simeq \sum_{i=0}^{n} \mu_i dN_i$ ---(5)

For equilibrium of the reaction, the change in Gibbs free energy of the system (equation (4)) should be considered. (L, added ligands such as triorganylphosphine oxide or oleylamine; G, Gibbs free energy; S, entropy; T, reaction temperature; V, volume of the system; P, pressure for the reaction; μ_i, chemical potentials of the chemical agents i where $\mu_i = dG / dN_i$) Because all of the nanocrystal growing reactions occur under the same temperature and atmospheric pressure, the total chemical potential change is almost equal to the change in Gibbs free energy of the reaction system (equation (5)).

The growth of nanosheets terminates at reaction equilibrium, and no significant growth occurs when the total chemical potentials for the reactants are the same, as determined by the sum of chemical potentials of unreacted reactants and those of the products (equations (6)-(7)). The chemical potentials of the ligand-passivated nanosheets as products can be rewritten as the chemical potentials of the consumed reactants (equation (8)):

$$dG = dG_f - dG_i = 0 \text{ ---(6)}$$

$$dG = [N_{unreacted}\, \Sigma\mu(\text{reactants}) + N_f * \Sigma\mu(MoSe_2\text{-}L)] - N_{initial}\, \Sigma\mu(\text{reactants}) = 0 \text{ ---(7)}$$

$$N_f * \Sigma\mu(MoSe_2\text{-}L) = N_{initial}\, \Sigma\mu(\text{reactants}) - N_{unreacted}\, \Sigma\mu(\text{reactants})$$

$$= (N_{initial} - N_{unreacted})\, \Sigma\mu(\text{reactants}) = N_{consumed}\, \Sigma\mu(\text{reactants}) \text{ ---(8)}$$

$N_{initial}$, molecular amounts of reactants such as Mo/Se precursors and ligands at the initial of reaction; $N_{unreacted}$, molecular amounts of unreacted reactants; N_f, number of nanosheets; μ(reactants), chemical potentials of the reactants; $\mu(MoSe_2\text{-}L)$, chemical potentials of the ligand-passivated $MoSe_2$ nanosheets as products.

When the ligands changed (e.g., TOPO and OLm) with the same reactants for nanosheet growth, the chemical potentials of the ligand-passivated nanosheets mainly affect the reaction direction since the chemical potentials of the metal-ligand complexes as reactants are expected to be similar according to TGA analysis (Figure S1). Considering that the chemical potentials consist of the crystal energy and surface energy,[3] the surface energy of the nanosheets during the nucleation and growth stages determines the morphologies of the nanosheets. In other words, the surface energies of the ligands, which originated from the ligand tail groups, determine the growth status of the nanosheets, such as dissolution or dispersion for growth of nanosheets in solution in our system.

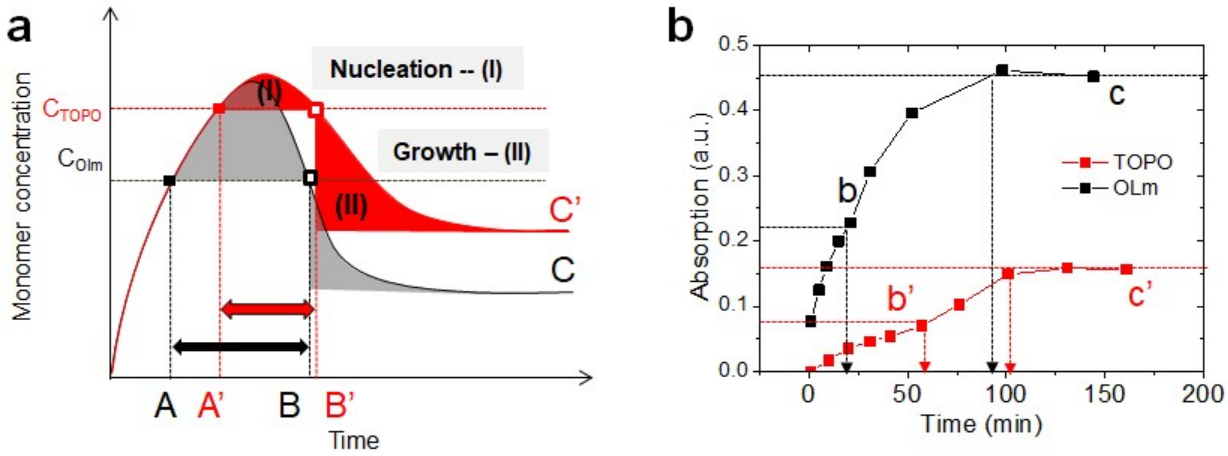

Figure S4. (a) Schematic representation of the LaMer diagram for nucleation and growth of $MoSe_2$-TOPO (red line) and $MoSe_2$-Olm (black line). (b) Absorption at 690 nm for the reaction solution in TOPO or Olm. All of the aliquots are extracted during the reaction and measured using the UV-vis absorption spectrum after diluting with chloroform.

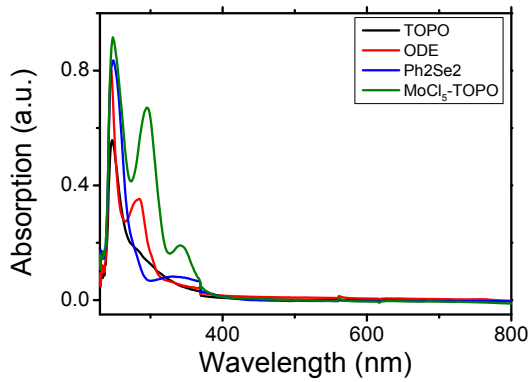

Figure S5. UV-vis absorption spectra of reagents for the synthesis of $MoSe_2$. All of the reagents were dissolved in $CHCl_3$

The absorbance spectra obtained from the precursors did not overlap with the absorbance of $MoSe_2$. Therefore, we concluded that the absorbance of diluted aliquots at 690 nm and 780 nm (as A and B excitons) could be used to determine the number of nanosheets

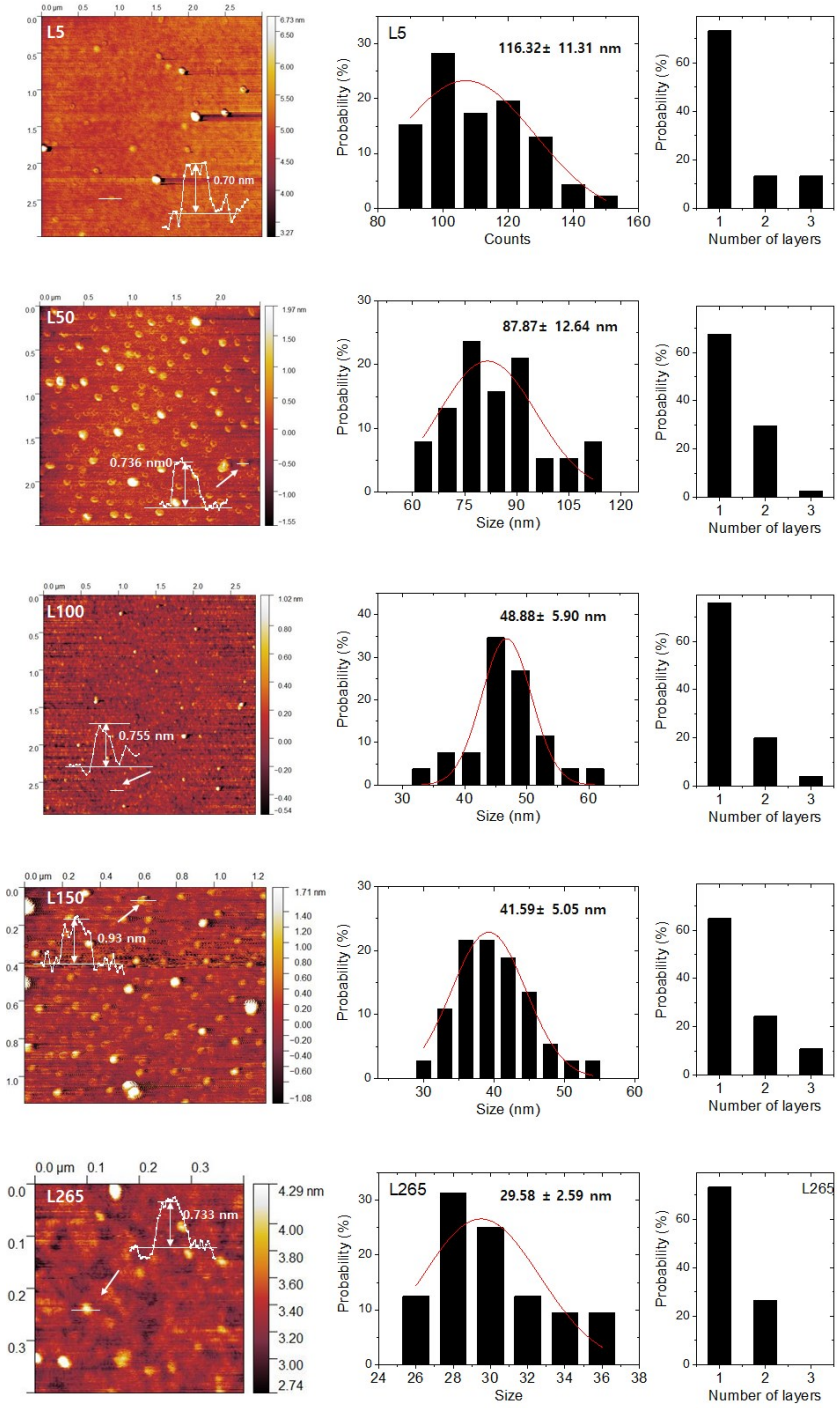

Figure S6. Atomic force microscopy (AFM) images of $MoSe_2$ synthesized with various concentrations of TOPO with insets of the height profile and corresponding distribution of the lateral size and height.

Considering that the thickness of the monolayer of $MoSe_2$, which is grown by chemical vapor deposition methods, is 0.71 nm,[2], the number of stacking layers of synthesized $MoSe_2$ is

calculated by (the observed height of the nanosheets in AFM) / (height of the $MoSe_2$ monolayer 0.71 nm).

Table S1. The height profiles for AFM analysis of $MoSe_2$ synthesized with various Ln of TOPO.

TOPO L5							
Entry	**Lateral size (nm)**	**Height (nm)**	**# of layers**	**Entry**	**Lateral size (nm)**	**Height (nm)**	**# of layers**
1	131.8	0.74	1.04	**16**	114.4	0.81	1.15
2	148.5	0.84	1.18	**17**	132.4	1.13	1.60
3	138.6	0.80	1.13	**18**	121.2	0.73	1.02
4	129.9	1.05	1.48	**19**	116	0.72	1.01
5	114.4	0.81	1.15	**20**	123.4	0.81	1.15
6	132.4	1.13	1.60	**21**	122.7	4.16	5.86
7	121.2	0.73	1.02	**22**	107.3	0.78	1.10
8	116	0.72	1.01	**23**	110.4	1.84	2.59
9	123.4	0.81	1.15	**24**	113.8	0.83	1.17
10	122.7	4.16	5.86	**25**	112.5	0.96	1.35
11	107.3	0.78	1.10	**26**	108.4	1.83	2.58
12	131.8	0.74	1.04	**27**	109.3	1.03	1.45
13	148.5	0.84	1.18	**28**	112.2	0.85	1.20
14	138.6	0.80	1.13	**29**	151.8	0.72	1.02
15	129.9	1.05	1.48	**30**	109.3	0.70	0.99
				Average	123.3	1.13	1.43
				standard deviation	12.7	0.85	0.69

TOPO L50							
Entry	**Lateral size (nm)**	**Height (nm)**	**# of layers**	**Entry**	**Lateral size (nm)**	**Height (nm)**	**# of layers**
1	69.9	1.21	1.71	**20**	106.7	0.79	1.11
2	64	0.86	1.22	**21**	78.2	0.73	1.03
3	93.1	0.95	1.34	**22**	94.4	1.06	1.49
4	95.2	0.71	0.99	**23**	80.5	1.04	1.47
5	71.9	0.63	0.89	**24**	98.2	0.78	1.10
6	97.3	0.88	1.24	**25**	77.8	1.28	1.80
7	75.7	0.75	1.05	**26**	118.3	1.50	2.11
8	72.2	1.02	1.44	**27**	78	0.82	1.15
9	87.4	1.45	2.04	**28**	83.7	1.00	1.40

10	93.6	0.68	0.95	**29**	114	1.32	1.86
11	66.9	0.70	0.99	**30**	87.8	0.87	1.22
12	89.8	1.36	1.91	**31**	76.5	0.74	1.04
13	99.4	1.31	1.84	**32**	98.8	1.43	2.01
14	87.9	1.40	1.96	**33**	96.7	1.00	1.40
15	79	0.82	1.16	**34**	95.5	1.41	1.98
16	82.7	0.92	1.30	**35**	93	0.91	1.28
17	77.4	0.77	1.08	**36**	108.9	1.10	1.54
18	89.4	1.86	2.61	**37**	94.3	0.73	1.03
19	89.8	0.73	1.02				
				Average	87.9	1.01	1.39
				standard deviation	12.6	0.29	0.47

TOPO L100							
Entry	**Lateral size (nm)**	**Height (nm)**	**# of layers**	**Entry**	**Lateral size (nm)**	**Height (nm)**	**# of layers**
1	40.9	1.34	1.89	**14**	43.3	0.63	0.89
2	46.2	0.78	1.10	**15**	39	0.65	0.91
3	55.5	0.74	1.05	**16**	57.7	1.34	1.89
4	48	0.75	1.05	**17**	47.1	0.73	1.02
5	53.2	0.91	1.28	**18**	51.2	1.15	1.62
6	52.4	0.93	1.30	**19**	49.9	0.98	1.38
7	47.3	0.73	1.03	**20**	36.2	0.69	0.97
8	49.3	0.69	0.97	**21**	46.5	0.65	0.92
9	48.3	1.03	1.45	**22**	49.6	0.76	1.06
10	52.8	1.40	1.98	**23**	46.5	0.84	1.18
11	50.8	0.87	1.23	**24**	56.5	1.29	1.82
12	46.8	0.80	1.12	**25**	64.9	1.72	2.43
13	43.7	1.03	1.45				
				Average	48.9	0.94	1.18
				standard deviation	5.9	0.28	0.55

TOPO L150							
Entry	**Lateral size (nm)**	**Height (nm)**	**# of layers**	**Entry**	**Lateral size (nm)**	**Height (nm)**	**# of layers**
1	50.5	1.71	2.41	**20**	36.7	0.75	1.05

2	38.1	0.69	0.97	**21**	43.4	0.73	1.03
3	44.2	0.71	0.99	**22**	44.2	0.96	1.35
4	32.8	0.77	1.08	**23**	38.4	1.05	1.47
5	41.1	0.84	1.18	**24**	45.5	0.69	0.97
6	33.2	0.71	1.01	**25**	40.2	0.70	0.98
7	40.1	1.11	1.56	**26**	43.1	0.81	1.14
8	41.7	1.82	2.56	**27**	44.3	0.85	1.19
9	37.8	0.74	1.04	**28**	46.6	1.74	2.45
10	45.5	1.30	1.83	**29**	44.2	0.97	1.36
11	43.5	1.92	2.71	**30**	34.1	0.87	1.23
12	34.9	0.72	1.01	**31**	38.9	0.80	1.12
13	35.9	0.81	1.14	**32**	36.6	0.71	1.01
14	37.4	1.18	1.66	**33**	40.8	1.27	1.79
15	40.9	0.89	1.25	**34**	48.1	1.34	1.89
16	41.4	0.78	1.09	**35**	51.4	1.34	1.88
17	56.6	2.23	3.14	**36**	42.1	0.82	1.15
18	46	2.03	2.86	**37**	42.5	1.15	1.62
19	38.8	0.81	1.15				
				Average	41.6	1.06	1.46
				standard deviation	5.0	0.42	0.64

L265							
Entry	**Lateral size (nm)**	**Height (nm)**	**# of layers**	**Entry**	**Lateral size (nm)**	**Height (nm)**	**# of layers**
1	26.61	1.73	2.43	**16**	28.7	0.72	1.02
2	29.07	0.94	1.33	**17**	27.73	0.75	1.05
3	27.63	1.05	1.48	**18**	28.8	1.55	2.18
4	30.2	0.84	1.18	**19**	29.3	0.89	1.26
5	33.15	1.58	2.22	**20**	33	1.21	1.70
6	25.46	0.63	0.88	**21**	30.9	0.71	1.00
7	30.68	0.71	1.00	**22**	27.4	2.16	3.04
8	28.6	0.70	0.99	**23**	29	0.99	1.39
9	28.925	1.02	1.44	**24**	32.7	0.82	1.15
10	27.1	1.86	2.62	**25**	31.4	1.52	2.14
11	27.84	1.03	1.44	**26**	33.3	1.22	1.72
12	26.35	1.42	2.00	**27**	31.79	1.05	1.48
13	26.23	1.02	1.43	**28**	29.03	1.87	2.64
14	37.48	0.84	1.18	**29**	27.9	1.29	1.81
15	31.8	1.24	1.75	**30**	29.2	2.02	2.84
				Average	29.6	1.18	1.56

				standard deviation	2.6	0.42	0.52

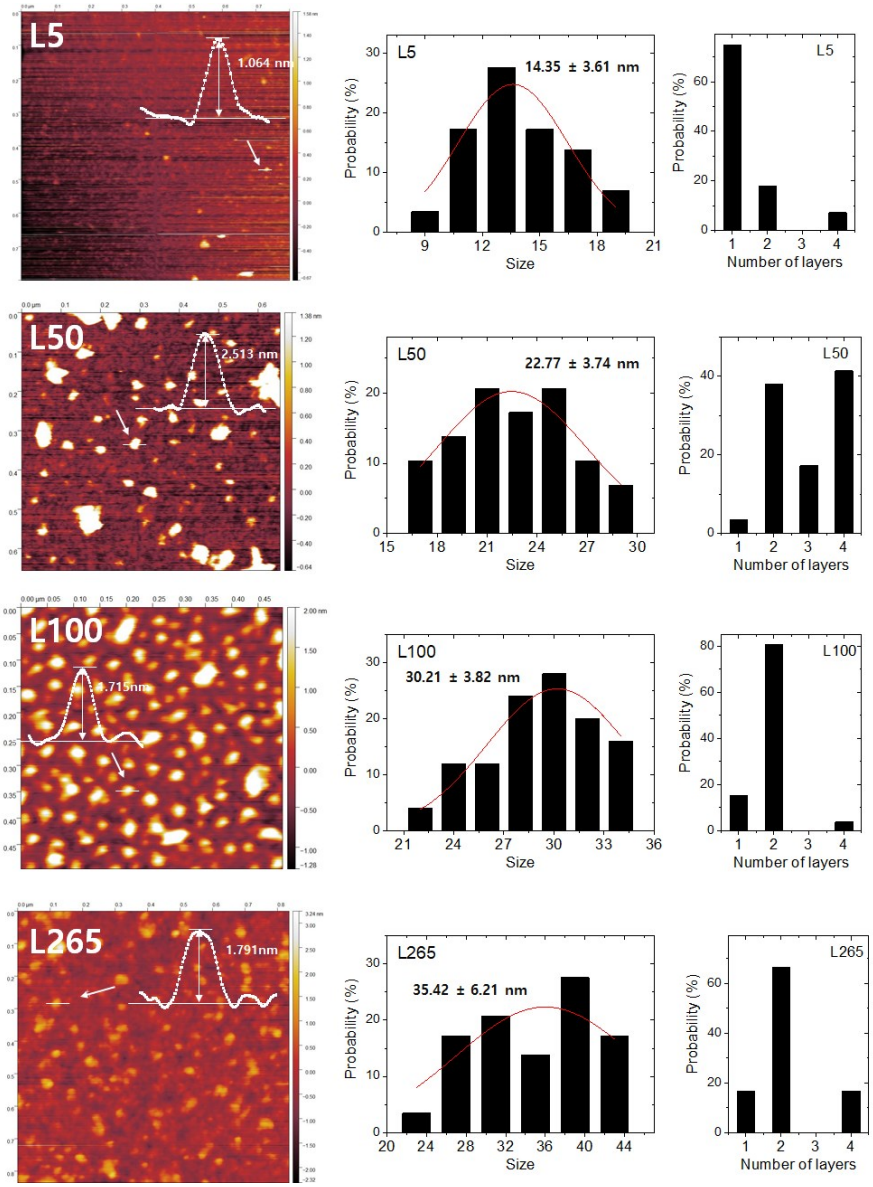

Figure S7. Atomic force microscopy (AFM) images of $MoSe_2$ synthesized with various concentrations of Olm with insets of the height profile and corresponding distributions of the lateral size and height.

Table S2. The height profiles for AFM analysis of $MoSe_2$ synthesized with various Ln of Olm.

Olm L5							
Entry	**Lateral size (nm)**	**Height (nm)**	**# of layers**	**Entry**	**Lateral size (nm)**	**Height (nm)**	**# of layers**
1	13.3	0.72	1.02	**14**	12.41	0.78	1.10
2	12.66	0.74	1.04	**15**	27.7	0.74	1.04
3	12.72	0.72	1.01	**16**	18.58	0.89	1.25
4	16.47	0.58	0.82	**17**	18.34	1.33	1.87
5	14.21	1.79	2.52	**18**	12.87	1.15	1.61
6	11.36	1.12	1.58	**19**	15.5	0.69	0.97
7	12.65	0.73	1.03	**20**	11.04	0.74	1.05
8	16.31	0.69	0.97	**21**	16.8	1.28	1.80
9	12.8	0.75	1.06	**22**	16.43	0.91	1.28
10	10.46	1.46	2.06	**23**	10.19	0.69	0.96
11	15.61	0.81	1.15	**24**	15.29	0.88	1.24
12	9.68	0.74	1.04	**25**	11.83	2.23	3.14
13	15.9	0.65	0.92	**26**	12.1	0.90	1.26
				Average	10.3	7.12	1.45
				standard deviation	5.0	9.35	0.53

Olm L50							
Entry	**Lateral size (nm)**	**Height (nm)**	**# of layers**	**Entry**	**Lateral size (nm)**	**Height (nm)**	**# of layers**
1	21.54	2.01	2.83	**16**	22.4	2.31	3.26
2	20.33	2.17	3.06	**17**	25	2.40	3.38
3	19.27	1.39	1.95	**18**	31.7	1.53	2.15
4	24.9	2.24	3.16	**19**	21.1	1.87	2.64
5	22.9	2.01	2.83	**20**	16.3	3.53	4.97
6	14.88	1.46	2.05	**21**	26	1.78	2.51
7	25.5	2.33	3.28	**22**	19.82	1.66	2.34
8	22.9	2.64	3.72	**23**	29.9	2.71	3.82
9	23.5	2.11	2.97	**24**	19.1	1.69	2.38
10	26.7	2.60	3.66	**25**	28.2	2.45	3.44
11	24.3	1.70	2.40	**26**	17.98	1.46	2.05
12	20	2.41	3.39	**27**	19.96	0.97	1.36
13	24.1	1.62	2.28	**28**	22.97	1.47	2.07
14	20.2	2.57	3.62	**29**	20.73	1.53	2.15
15	24.7	2.51	3.54	**30**	26.26	1.54	2.17

				Average	22.8	2.02	2.85
				standard deviation	3.7	0.53	0.75

Olm L100							
Entry	**Lateral size (nm)**	**Height (nm)**	**# of layers**	**Entry**	**Lateral size (nm)**	**Height (nm)**	**# of layers**
1	26.61	1.00	1.40	**17**	27.64	1.34	1.88
2	28.9	1.20	1.69	**18**	29.27	1.71	2.41
3	27.95	1.50	2.11	**19**	34.1	1.89	2.66
4	31.34	1.54	2.16	**20**	31.6	1.62	2.29
5	29.63	1.74	2.45	**21**	26.92	1.06	1.50
6	30.98	2.02	2.85	**22**	29.02	1.69	2.39
7	23.88	1.00	1.40	**23**	35.37	2.15	3.03
8	31.4	2.04	2.87	**24**	29.37	1.41	1.99
9	32.56	1.72	2.42	**25**	27.64	1.50	2.12
10	33.7	2.11	2.97	**26**	31.59	1.46	2.06
11	37.3	2.12	2.99	**27**	23.9	1.28	1.80
12	29.27	1.47	2.07	**28**	29.76	1.71	2.41
13	27.85	1.48	2.09	**29**	24.19	1.44	2.03
14	21.87	0.74	1.04	**30**	27.95	1.72	2.42
15	36.34	1.56	2.20	**31**	26.59	1.21	1.70
16	33.43	1.50	2.11	**32**	34.27	2.11	2.97
				Average	30.2	1.56	2.20
				standard deviation	3.8	0.38	0.54

L265							
Entry	**Lateral size (nm)**	**Height (nm)**	**# of layers**	**Entry**	**Lateral size (nm)**	**Height (nm)**	**# of layers**
1	26.3	1.26	1.77	**16**	32.2	1.44	2.02
2	35.98	1.82	2.56	**17**	49.9	1.86	2.62
3	26.22	1.39	1.96	**18**	38.9	1.19	1.67
4	38.4	1.45	2.04	**19**	35.1	1.52	2.14
5	37.4	1.78	2.50	**20**	43.6	1.43	2.02
6	30.61	1.70	2.39	**21**	37.4	1.76	2.48
7	35.61	1.48	2.08	**22**	40.2	1.92	2.70
8	36.4	1.47	2.07	**23**	38.17	1.13	1.59

9	30.9	1.76	2.48	**24**	40.5	0.92	1.30
10	43.1	1.29	1.82	**25**	30	1.42	2.00
11	38.1	0.86	1.22	**26**	41.71	1.66	2.34
12	31.9	1.18	1.67	**27**	24.7	0.84	1.18
13	26.46	1.35	1.90	**28**	43.5	1.68	2.36
14	41.9	1.79	2.52	**29**	28.2	0.68	0.96
15	31.6	1.12	1.58	**30**	27.82	0.69	0.98
				Average	35.4	1.39	1.90
				standard deviation	6.2	0.35	0.59

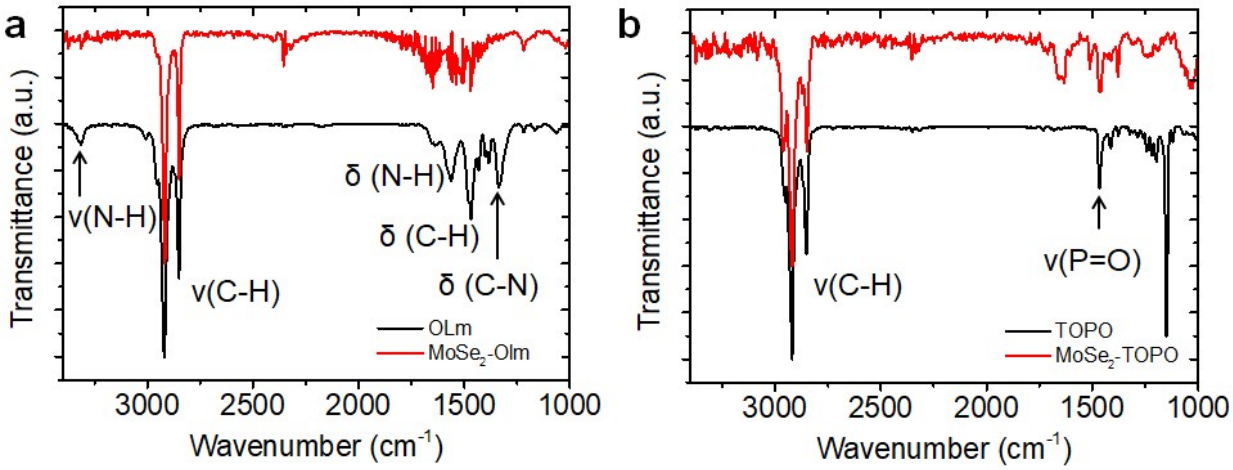

Figure S8. FTIR spectra of the synthesized $MoSe_2$ nanosheets with (a) TOPO and (b) Olm.

Fourier transform infrared (FTIR) spectroscopy was used to observe the existence of the surface-bound ligands. The $MoSe_2$ nanosheets synthesized with oleylamine show the C-H stretch vibration peak and weakening or even disappearance of N-H stretching, as well as N-H, C-N bending vibrations in Figure S8a. This can be attributed to the strong interactions of amine functional groups with the $MoSe_2$ nanosheets.

On the other hand, in the case of $MoSe_2$ synthesized with TOPO, the C-H stretch vibration peak is shown in the range of 2800-3000 cm^{-1}. The functional group-related P=O stretch vibration peak is observed at 1461 cm^{-1}, which is slightly redshifted compared to the TOPO molecules

(1465 cm^{-1}). This can be ascribed to the weak interactions between the TOPO and the $MoSe_2$ nanosheets.

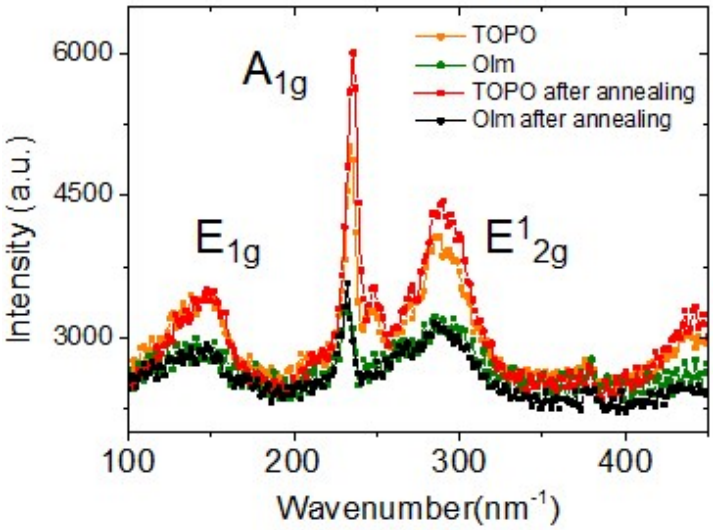

Figure S9. Raman scattering spectra of the $MoSe_2$ nanosheets synthesized with Olm and TOPO. The characteristic E_{1g}, A_{1g} and E^1_{2g} vibrations for the 2H $MoSe_2$ are observed without any different phases of $MoSe_2$.[3]

Table S3. XPS of the Mo 3d core level

		Mo^{4+}-Se		Mo^{4+}-L		Mo^{6+}	
		Mo 3d $_{5/2}$	Mo 3d $_{3/2}$	Mo 3d $_{5/2}$	Mo 3d $_{3/2}$	Mo 3d $_{5/2}$	Mo 3d $_{3/2}$
Olm	**Binding energy (eV)**	228.82	231.92	229.55	232.65	232.63	235.73
	Relative area (%)	48.31	26.78	8.19	4.27	7.21	5.25
TOPO	**Binding energy (eV)**	228.98	232.11	230.05	233.15		
	Relative area (%)	57.74	33.90	5.84	2.53		

Table S4. XPS of the Se 3d core level

		Se 3d $_{5/2}$	Se 3d $_{3/2}$
Olm	**Binding energy (eV)**	54.25	55.10
	FWHM (eV)	48.31	0.90
TOPO	**Binding energy (eV)**	54.40	55.24
	FWHM (eV)	0.81	0.90

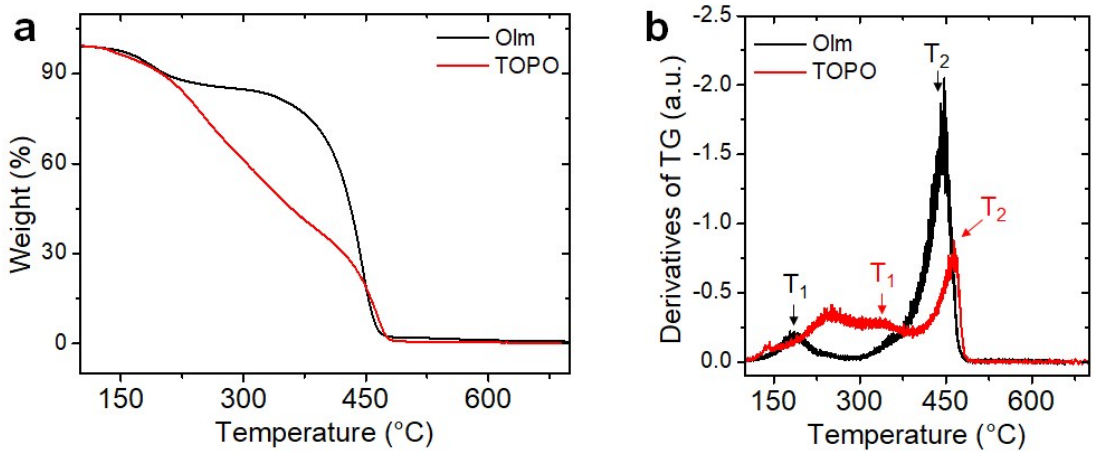

c

	Molecular weight (g/mol)	Boiling Point (°C)	T_1 (°C)	Weight loss at T_1 (%)	T_2 (°C)	Weight loss at T_2 (%)	Chemisorbed ligands (mmol/g)
TOPO	386.65	408.80	337.69	50.73	463.59	21.27	0.55
Olm	267.49	364	188.51	7.47	447.28	64.53	2.41

Figure S10. Thermogravimetric (TG) spectra of the $MoSe_2$ nanosheets synthesized with different organic ligands. (a) TG and (b) derivatives of TG (DTG).

The percentage of weight loss of ligand-adsorbed nanosheets is measured with increases of 10 °C/min under an N_2 atmosphere to confirm the amounts of chemisorbed ligands. The temperature at which organic ligands detach from the surface is analyzed using the first derivatives of the TG spectra, as shown in Figure S10b. The inflection point of weight loss is considered as the temperature at which ligands are detached. The lower temperature of weight loss (T_1) represents desorption of the physisorbed ligands, and the higher temperature of weight loss (T_2) represents chemisorbed ligands from the nanosheets. The amounts of chemisorbed ligands per weight can be calculated as below:

The amount of chemisorbed ligands (mmol/g) = 1g of materials x weight loss percentage at T_2 (%) / molecular weight of ligands (g/mol) x (1000 mmol / 1 mol)

In partial conclusion, the amounts of TOPO as ligands are adsorbed 4.38 times less than those of Olm.

Figure S11. Photograph of the colloidal nanosheets solution in $CHCl_3$. The Tyndall effects are presented, indicating that the synthesized nanosheets retain high colloidal stability over three months.

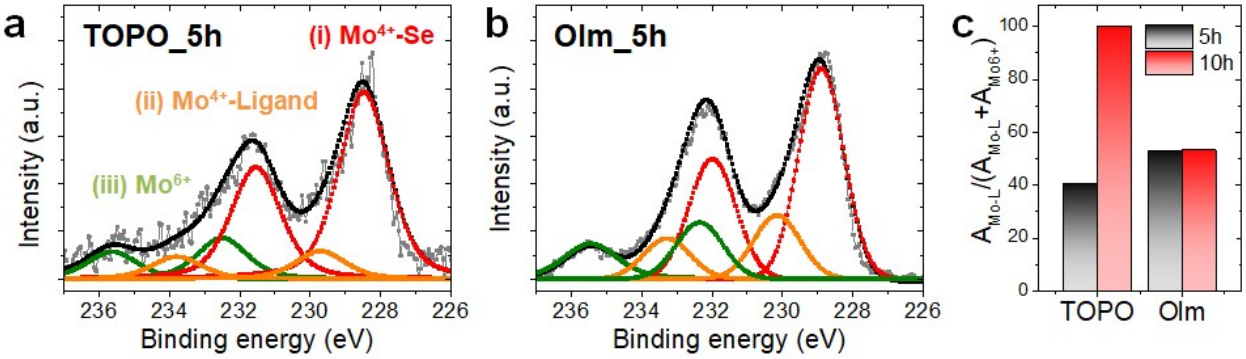

Figure S12. The XPS spectra of $MoSe_2$ nanosheets grown for 5h with (a) TOPO and (b) Olm. The ratio of Mo-L chemical species to the sum of the Mo-L and Mo^{6+} species depending on the reaction time (c). $A_{Mo\text{-}L}$ indicates the area of Mo-L species of Mo $3d_{5/2}$ orbitals, and A Mo^{6+} represents the area of Mo^{6+} species of Mo $3d_{5/2}$ orbitals.

Supplementary note 3:

Detailed calculation methods

The present first principle DFT calculations are performed using the Vienna Ab initio Simulation Package (VASP)[7] with the projector augmented wave (PAW) method.[8] The exchange-functional is treated using the generalized gradient approximation (GGA) of the Perdew-Burke-Ernzerhof (PBE) functional.[7] The cut-off energy of the plane-wave basis is set at 450 eV for optimizing the calculations for atom and cell optimization. The vacuum spacing in a direction perpendicular to the plane of the catalyst is at least 15 Å. Brillouin zone integration is performed using 3×3×1 Monkhorst-Pack k-point sampling for a primitive cell.[9] The self-consistent calculations utilize a convergence energy threshold of 10^{-5} eV. The equilibrium lattice constants are optimized with the maximum stress on each atom within 0.03 eV/Å. Grimme's DFT-D3 methodology was used to describe the dispersion interactions among all atoms in the polyimide unit cell and adsorption models of interest.[10,11] In addition, the concentration of molecules is defined as the ratio of molecules to surface Mo in the surface structure.

The **adsorption Energies** (Eads) are given by:

$$Eads = E_{surface+ligand} - E_{surface} - E_{ligand},$$

where $E_{surface}$+ligand is the total energy of a given surface and one attached molecule per supercell, $E_{surface}$ is the energy of the surface, and E_{ligand} is the energy of the capping ligand.

The **surface Energies** are given by:

$$\sigma_{surface} = E(slab)_{total} - n_{Mo}\mu_{Mo} - n_{Se}\mu_{Se} - n_{molecules}(\mu_{molecules})_{liquid} / A$$

where $E(slab)_{total}$ is the total energy of the surface, n_{Mo} and n_{Se} are the numbers of Mo and Se atoms in the surface, respectively, μ_{Mo} and μSe are their respective chemical potentials in bulk, $n_{molecules}$ is the number of molecules in the supercell, and $(\mu_{molecules})_{liquid}$ is the estimated chemical potential of the molecules in the liquid state.

Table S5. The surface energies of different facets in $MoSe_2$ depending on ligand coverage of trimethylphosphinine oxide (Me_3PO) and methylamine ($MeNH_2$). The energies are in units of eV $Å^{-2}$

Coverage efficiency (%)			0	10	40	70
Surface energies (eV $Å^{-2}$)	(001)	$MeNH_2$	-0.615	-0.871	-0.325	0.113
		Me_3PO	-0.615	-1.139	0.731	0.327
	(110)	$MeNH_2$	0.093	0.021	0.037	0.047
		Me_3PO	0.093	0.069	0.062	0.632
	(100)	$MeNH_2$	0.145	-0.075	0.091	0.109
		Me_3PO	0.145	-0.126	-0.042	0.082

(001) facets

Coverage percentage (%)	12.5	37.5	75
Methylamine	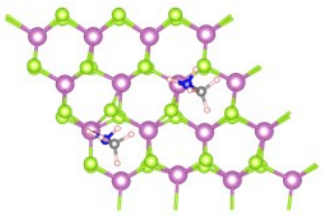	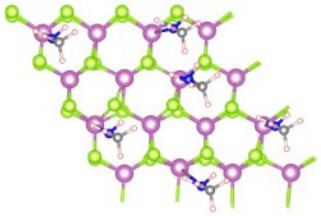	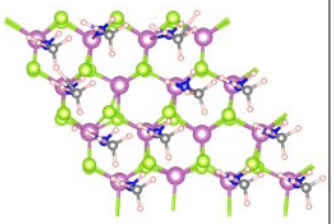
Trimethyl phosphine oxide	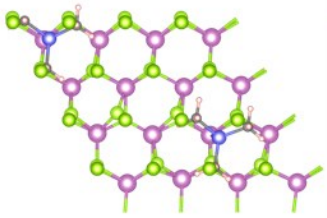	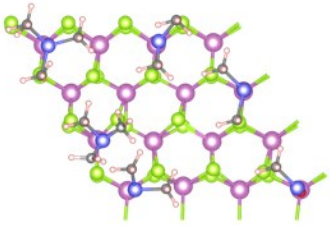	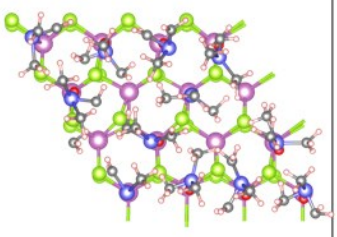

(110) facets

Coverage percentage (%)	16.7	33.3	66.7
Methylamine	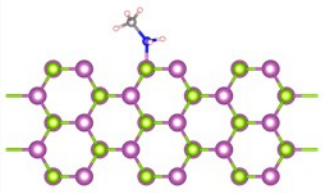	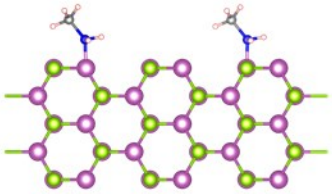	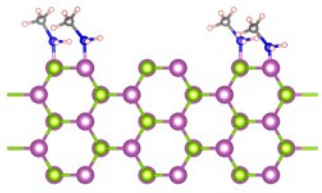
Trimethyl phosphine oxide	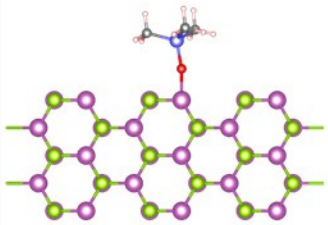	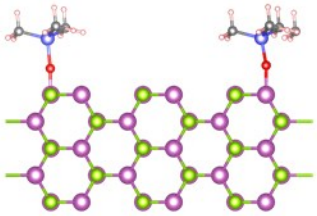	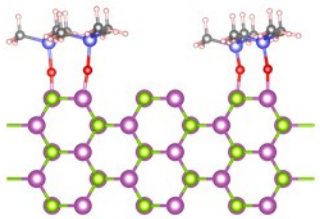

(100) facets

Coverage percentage (%)	12.5	37.5	75
Methylamine	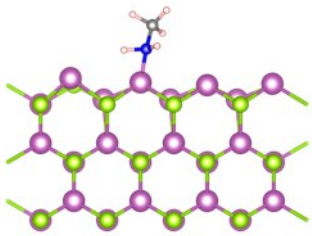	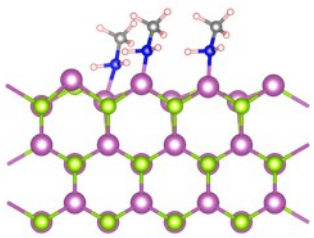	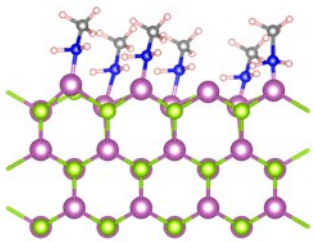
Trimethyl phosphine oxide	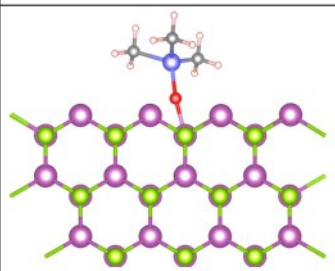	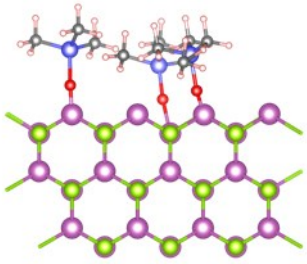	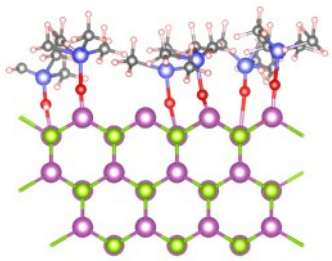

Figure S13. Model structure for calculations of the surface energies in accordance with the ligand coverage percentage.

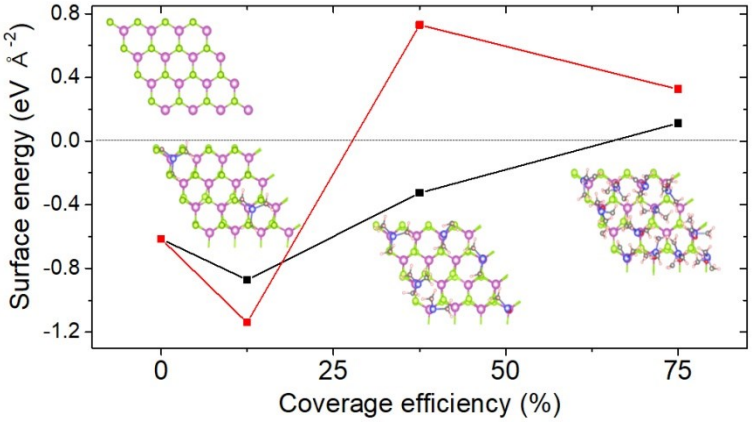

Figure S14. The surface energies of (001) facets as a function of the ligand coverage percentage. The red lines correspond to the adsorption of methylphosphine oxide, and the black line is related to the adsorption of methylamine.

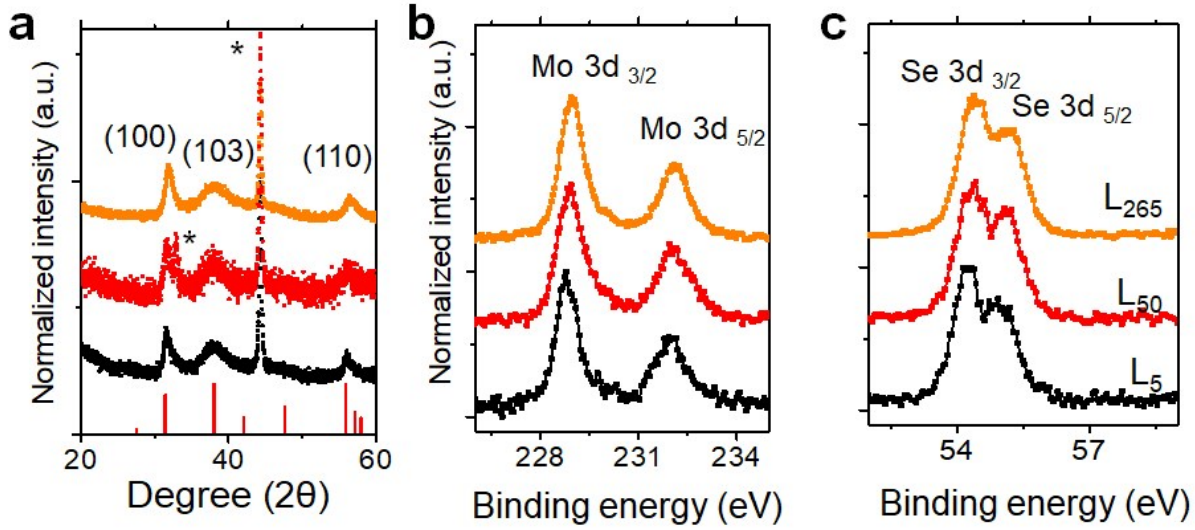

Figure S15. (a) XRD spectra of the corresponding $MoSe_2$ nanosheets with L5, L100, and L265 of TOPO. The spectra are referenced to JCPDF No. 15-29, where * indicates the peaks of SiO_2 used as the substrate. (b) and (c) XPS spectra of Mo 3d and Se 3d, respectively, for the corresponding $MoSe_2$ nanosheets.

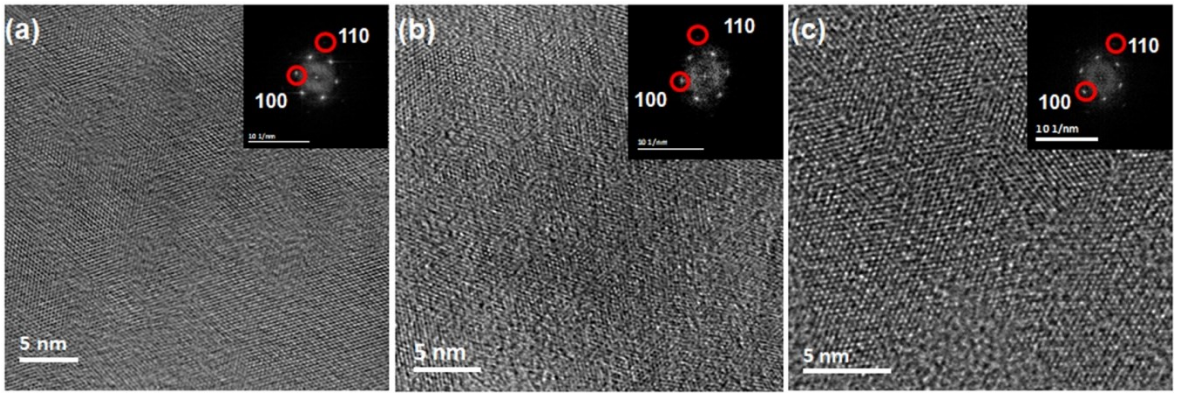

Figure S16. (a-c) HRTEM images of the $MoSe_2$ synthesized with L5, L50, and L265, respectively. The insets are the reduced fast Fourier transformed images, which are comparable to hexagonal $MoSe_2$. The (110) and (100) planes with a zone axis of [10-1] are shown in the rFFT.

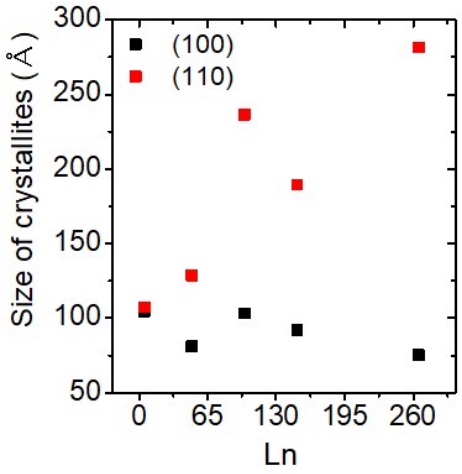

Figure S17. The crystalline sizes along the (100) and (110) facets according to Ln.

As Ln increases, the crystalline sizes of the (100) facets are very similar, whereas the crystalline sizes of the (110) facets continually increase. The obtained crystalline sizes of the nanosheets are larger than the Bohr radius of $MoSe_2$, 2.40 nm.[12] Besides, previous studies by Jin et al. demonstrated that the photoluminescence of WSe_2 was blue-shifted due to quantum-confinement effects.[13] However, the absorption spectrum was not changed. Thus, the blue-shifted absorption peaks of the A exciton with increasing ligand concentration are attributed to thickness-dependent properties rather than lateral size confinements.

Table S6. The crystalline size of $MoSe_2$ synthesized with different concentration of TOPO, Ln.

	(100) facet			(110) facet		
	angle, 2θ	fwhm, Δ(2θ)	crystallites' radius, Å	angle, 2θ	fwhm, Δ(2θ)	crystallites' radius, Å
L5	31.60	0.79	104.51	56.59	0.84	107.41
L50	31.84	1.02	80.99	56.30	0.7	128.71
L100	31.62	0.8	103.21	55.80	0.38	236.56
L150	31.90	0.9	91.80	6.22	0.42	189.43
L265	31.78	1.1	75.09	56.32	0.32	281.59

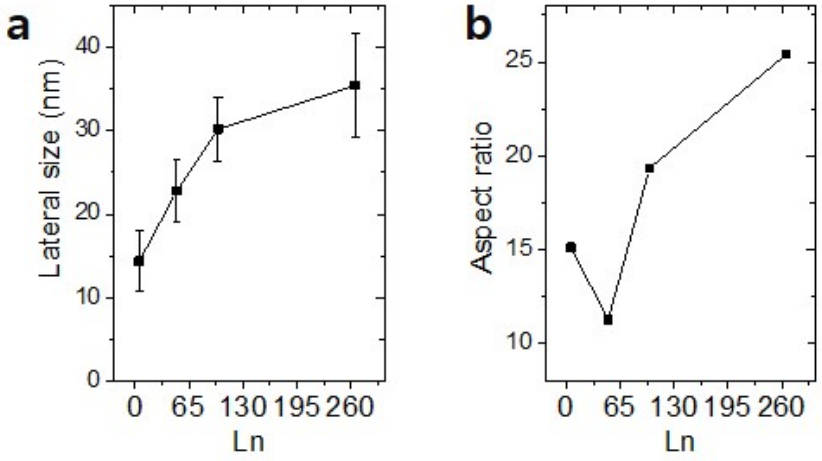

Figure S18. Plot of the average lateral size of the $MoSe_2$ nanosheets synthesized with Olm (a) and the aspect ratio (b), as observed through AFM analysis. The lateral size and aspect ratio of the nanosheets synthesized with Olm have an inverted tendency compared to those with TOPO.

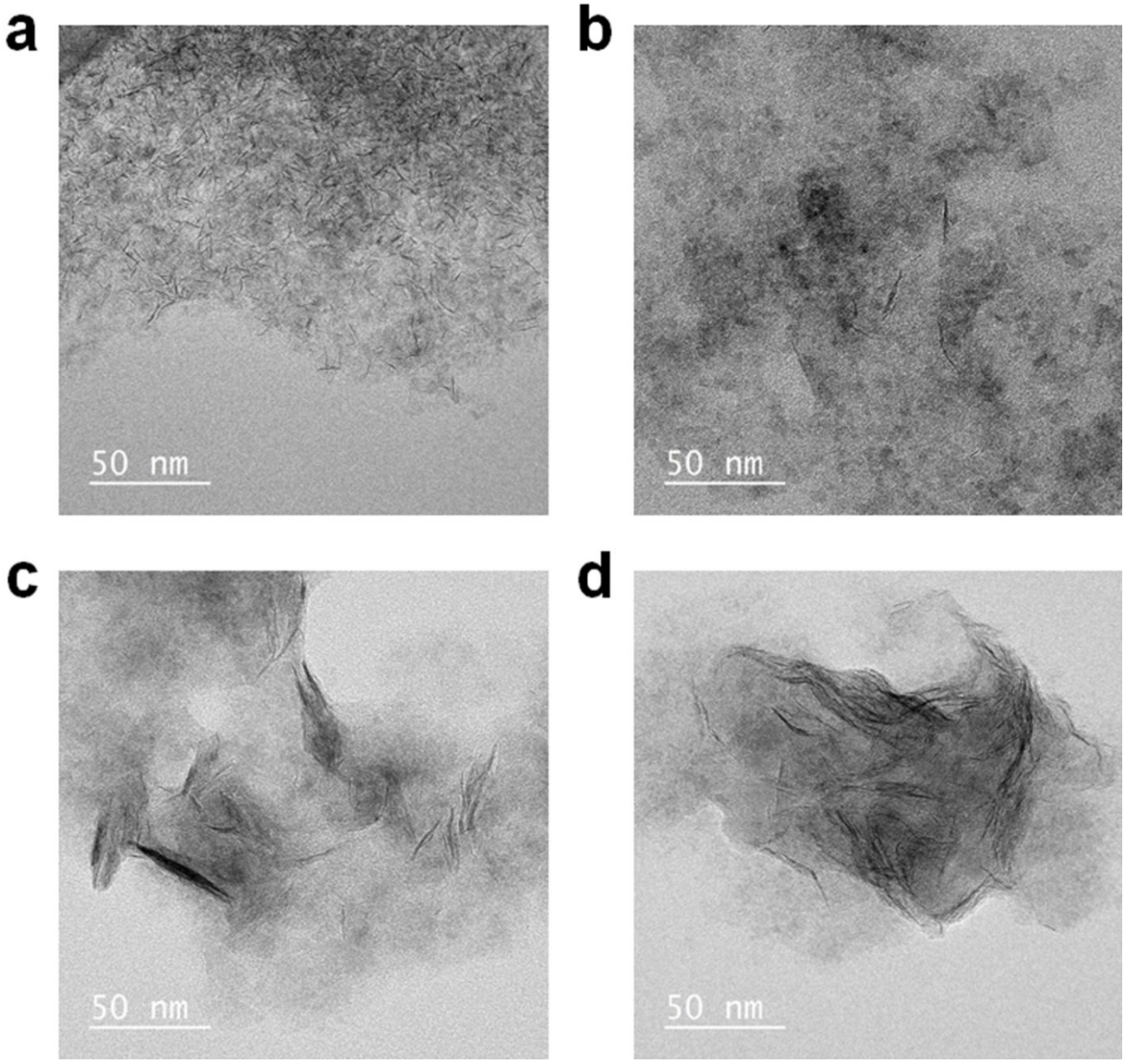

Figure S19. TEM images of $MoSe_2$ synthesized with aliphatic ligands. $MoSe_2$ nanosheets were synthesized with an L-type ligand, oleylamine, with (a) 5 equivalents to the metal precursor ($MoCl_5$) and (b) 265 equivalents to the metal precursor ($MoCl_5$). $MoSe_2$ nanosheets were grown with (c) 5 and (d) 265 equivalents of X-type oleic acid compared to the metal precursor ($MoCl_5$).

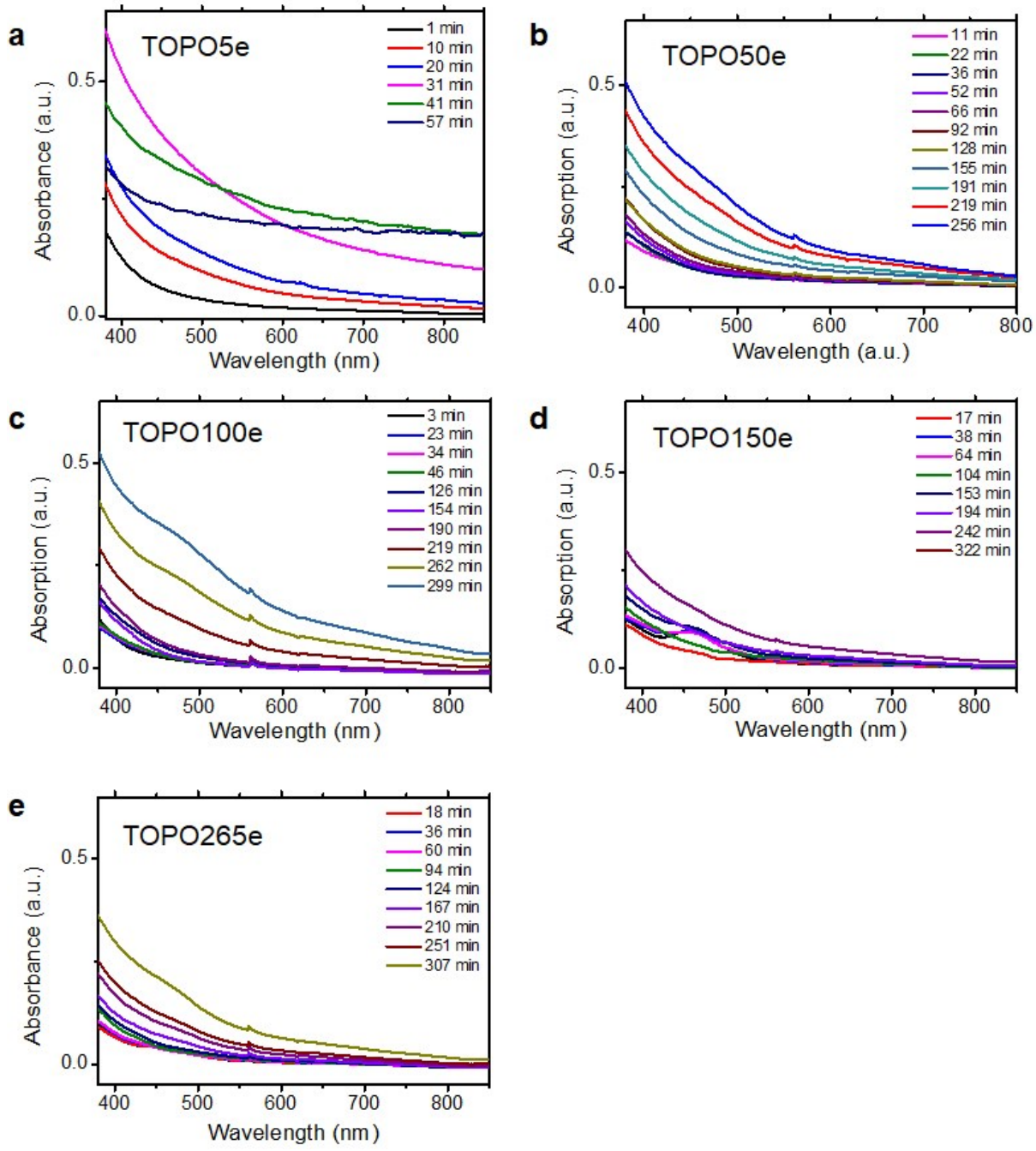

Figure S20. UV-vis spectra of aliquots with (a-e) different amounts of TOPO extracted as a function of time.

Table S7. Quantitative analysis of the remaining precursors after reaction as a function of the concentration of TOPO as determined by X-ray fluorescence spectroscopy.

	Equivalent to metal precursors	5	50	100	150	265
Weight % in supernatant	**P**	0.867	5.42	9.969	13.74	18.53
	Se	0.609	2.543	3.07	2.67	2.759
	Mo	0.182	1.286	1.669	1.584	1.391
molar amounts in supernatant	**P (mmol)**	0.13134	0.8933	1.76243	2.59366	4.05545
	Se (umol)	0.03619	0.16441	0.2129	0.19771	0.23687
	Mo (umol)	0.0089	0.06843	0.09526	0.09653	0.09828

All supernatants obtained from the centrifugation purification process were concentrated to remove hexane and 2-propanol (used as washing solvents), which have lower boiling points than the reagents used in the reaction. These samples were used for elemental analysis to verify the amounts of unreacted precursors after synthesis. The weight percentages of each element were calculated under the assumption that only P, Se, and Mo elements exist in the supernatants. Then, the molar amount was determined as (total mass of reaction solution * weight% / atomic weight) to compare the remaining amounts of elements depending on the concentration of TOPO as a capping ligand.

As the ratio of TOPO to $MoCl_5$ increased, the number of TOPO ligands coordinating with the Mo/Se elements increased. This process reduced the chemical potential of the Mo/Se elements, decreasing the activity of Mo/Se elements in the growth of $MoSe_2$. The coordination of TOPO to the Mo/Se elements was saturated at ligand ratios above L100.

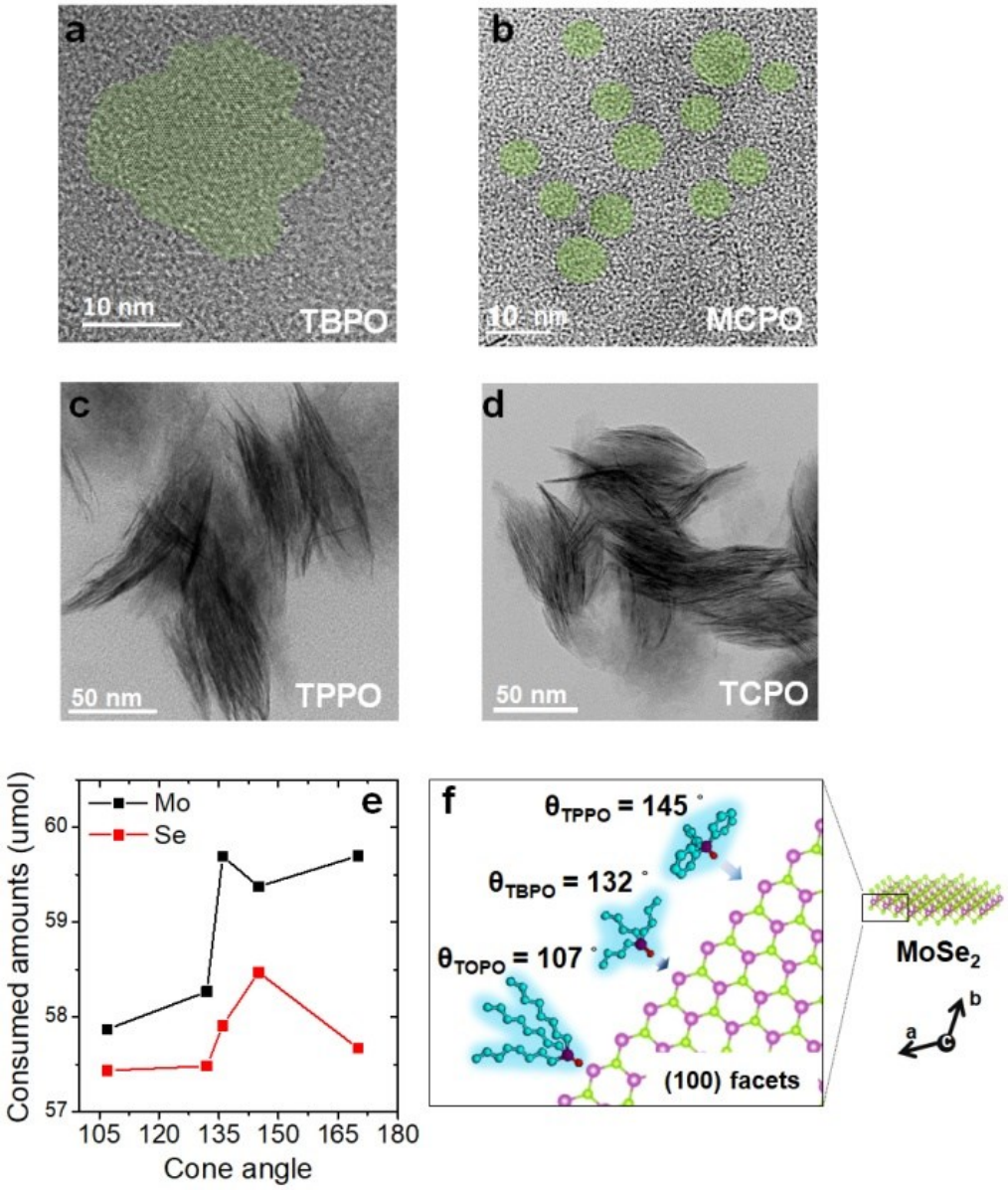

Figure S21. TEM images of $MoSe_2$ synthesized with L100 of ligands in the composition of TOPO: phosphine oxide ligands, which have various cone angles (a) TBPO, (b) MCPO, (c) TPPO, and (d) TCPO as 9:1. (e) The respective consumed amounts of precursors at each condition as measured by XRF. (f) Illustration of the ligand accessibilities of the ligands on the (100) facets of the $MoSe_2$. The cone angle indicates the coverage of the surface of the nanosheets to screen the surface dipole, which is induced by the adsorption of ligands.

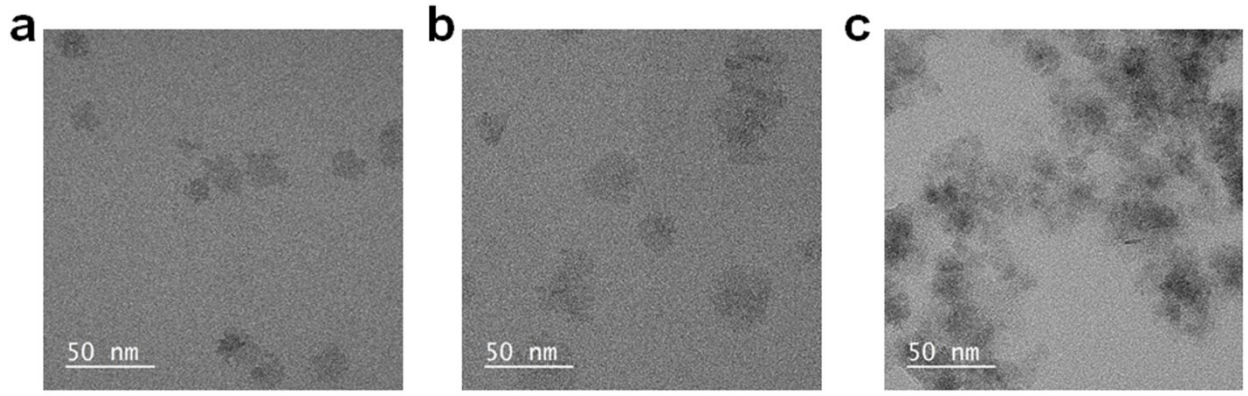

Figure S22. TEM images of $MoSe_2$ nanosheets synthesized with 265 equivalents of TOPO for the amounts of chalcogen ions produced by phenyldiselenide: (a) 1 equivalent, (b) 2 equivalents, and (c) 4 equivalents to the metal ions.

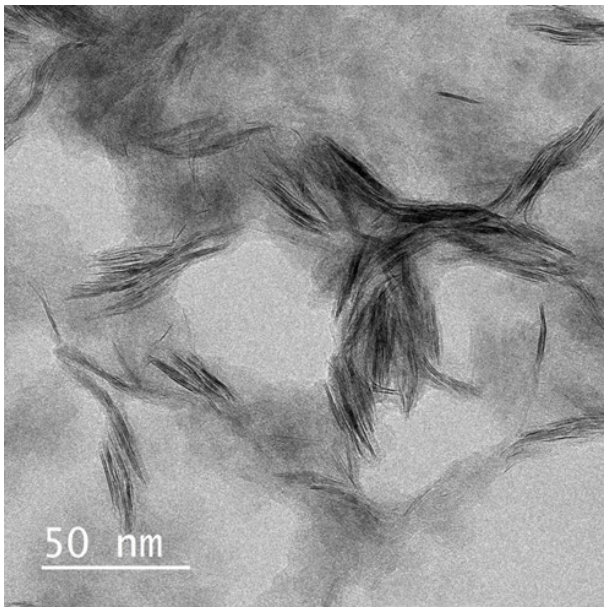

Figure S23. HRTEM images of $MoSe_2$ synthesized at 330 °C for 10 hours, with 265 equivalents of TOPO.

$MoSe_2$ grown at a higher temperature (330°C) showed a decreased size and increased thickness. $MoSe_2$ synthesized with L_{265} at 330°C showed a decreased size (26.8 ± 4.6 nm) and increased number of stacking layers (3.8 ± 0.3) compared to $MoSe_2$ synthesized at 280°C (Figure 2c).

1. A. A. Maryott and E. R. Smith, *Table of dielectric constants of pure liquids*, U.S. Govt. Print. Off., 1951.
2. J. Xia, X. Huang, L.-Z. Liu, M. Wang, L. Wang, B. Huang, D.-D. Zhu, J.-J. Li, C.-Z. Gu and X.-M. Meng, *Nanoscale*, 2014, **6**, 8949-8955.
3. N. T. K. Thanh, N. Maclean and S. Mahiddine, *Chem. Rev.*, 2014, **114**, 7610-7630.
4. U. Gupta, B. S. Naidu, U. Maitra, A. Singh, S. N. Shirodkar, U. V. Waghmare and C. N. R. Rao, *APL Mater.*, 2014, **2**, 092802.
5. S.-H. Su, W.-T. Hsu, C.-L. Hsu, C.-H. Chen, M.-H. Chiu, Y.-C. Lin, W.-H. Chang, K. Suenaga, J.-H. He and L.-J. Li, *Front. Energy Res.*, 2014, **2**.
6. W. Jung, S. Lee, D. Yoo, S. Jeong, P. Miró, A. Kuc, T. Heine and J. Cheon, *J. Am. Chem. Soc.*, 2015, **137**, 7266-7269.
7. J. P. Perdew, K. Burke and M. Ernzerhof, *Phys. Rev. Lett.*, 1996, **77**, 3865-3868.
8. G. Kresse and D. Joubert, *Phys. Rev. B*, 1999, **59**, 1758-1775.
9. H. J. Monkhorst and J. D. Pack, *Phys. Rev. B*, 1976, **13**, 5188-5192.
10. L. Gong, D. Zhang, C.-Y. Lin, Y. Zhu, Y. Shen, J. Zhang, X. Han, L. Zhang and Z. Xia, *Adv. Energy Mater.*, 2019, **9**, 1902625.
11. S. Grimme, J. Antony, S. Ehrlich and H. Krieg, *J. Chem. Phys.*, 2010, **132**, 154104.
12. G. Wang, I. C. Gerber, L. Bouet, D. Lagarde, A. Balocchi, M. Vidal, T. Amand, X. Marie and B. Urbaszek, *2D Mater.*, 2015, **2**, 045005.
13. H. Jin, M. Ahn, S. Jeong, J. H. Han, D. Yoo, D. H. Son and J. Cheon, *J. Am. Chem. Soc.*, 2016, **138**, 13253-13259.